

# Mode-specific quantum rate effects for interfacial electron transfer: Computational case studies based upon 4-cyano-*N*-methylpyridinium reduction

Donald C. Selmarten and Joseph T. Hupp\*

Department of Chemistry, Northwestern University, Evanston, IL 60208, USA

Multi-mode quantum rate theory is used to examine the interfacial kinetics of a prototypical organic-radical-generating reaction: the reduction of the 4-cyano-*N*-methylpyridinium cation. Charge-transfer-enhanced Raman scattering experiments (R. L. Blackburn, *et al.*, *J. Phys. Chem.*, 1991, **95**, 10535) previously showed that 13 vibrational modes are coupled to the reduction process. From a time-dependent analysis of the scattering spectrum, precise coordinate displacement and reorganizational parameters for each of the modes have now been determined. These parameters, when incorporated into the rate theory, have yielded an extremely detailed—perhaps unprecedented—description of electrochemical reaction kinetics, including complete descriptions of: (a) mode-specific barrier effects, (b) mode-specific tunnelling effects, (c) non-classical activation effects and (d) sum-over states driving force effects.

It is generally accepted that rates of electron transfer (ET) at electrochemical interfaces are governed by dynamical effects (pre-exponential effects) together with activation barrier effects (exponential effects). Dynamical effects can reflect either rate-limiting electronic coupling effects ('non-adiabatic' reaction kinetics) or rate-limiting nuclear motion (solvental or vibrational dynamics; 'adiabatic' reactivity). Numerous examples of both adiabatic and non-adiabatic behaviour have now been documented and several insightful reviews have recently appeared.<sup>1–5</sup> Although dynamical effects clearly are important, our focus here is on barrier phenomena, with a particular emphasis on mode-specific vibrational effects. Much like adiabatic dynamical effects, barrier effects exist because of differences in solvation energy for oxidized and reduced species and differences in internal molecular structure (*i.e.*, bond length and bond angle differences or, equivalently, normal coordinate displacements).<sup>6–8</sup> In contrast to pre-exponential effects, they are usually strongly dependent on temperature and electrochemical potential, at least under conditions of low to intermediate driving force.

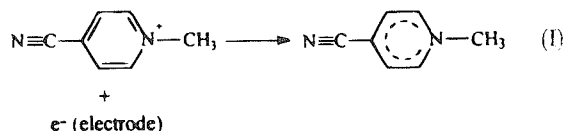
A quantitative understanding of barrier effects (and overall rate effects) for any particular reaction obviously requires a quantitative knowledge of the magnitude of the factors contributing to the barrier. Solvent barrier effects typically have been estimated *via* theoretical modelling or, less commonly, by experimentally varying a key parameter such as the reactant to electrode separation distance<sup>5,9</sup> or the reactant size.<sup>10</sup> Vibrational barrier heights, on the other hand, have most often been derived from X-ray crystallographic or solution EXAFS measurements of reactant and product bond-lengths. Bond-length differences (ET-induced local coordinate displacements,  $\Delta\alpha$ ) can be combined with local-mode force constants,  $f$ , to yield classical vibrational barrier heights,  $\Delta G_{\text{vib}}^*(\text{class})$ , under exchange conditions (zero driving force conditions):<sup>6–8</sup>

$$\Delta G_{\text{vib}}^*(\text{class}) = (1/4)bf(\Delta\alpha)^2 = \chi_{\text{vib}}/4 \quad (1)$$

In eqn. (1),  $b$  is the number of equivalent bonds undergoing displacement and  $\chi_{\text{vib}}$  is the vibrational portion of the Marcus reorganization energy. If more than one type of bond changes length upon ET then eqn. (1) additionally includes an appropriate summation.

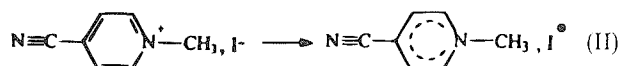
The X-ray approach and eqn. (1) are most readily applic-

able when: (a) both redox forms are stable, (b) the number of bond types is small, and (c) local modes can easily be related to normal modes. High-symmetry metal complexes such as octahedral aquo-complexes are representative of systems for which this approach works well.<sup>11,12</sup> In contrast, organic-radical-generating redox reactions such as reaction (I) can present real difficulties for the traditional X-ray approach, not only because of chemical irreversibility (structurally unstable product states), but also because of the vibrational complexity inherent to charge transfer to or from aromatic  $\pi$  or  $\pi^*$  type systems. Recently we showed that an alternative methodology based on a time-dependent analysis of resonance Raman spectra<sup>13–16</sup> could be used to assess vibrational reorganizational barriers for these kinds of systems.<sup>17</sup> The alternate approach requires the generation of an optical charge transfer transition that is functionally equivalent to the electrochemical reaction. Specifically for reaction (I) we have observed that the combination of iodide as an electron donor and *N*-methyl-4-cyanopyridinium as an electron acceptor yields an appropriate visible region ( $\lambda_{\text{max}} = 428 \text{ nm}$ ) transition:<sup>17–19</sup>



The availability of an accessible charge transfer transition provides a basis for resonance enhancement of Raman scattering. A key point, however, is that enhancement effects arise only for those vibrational modes that experience a net displacement upon charge transfer.<sup>13–17</sup> A time-dependent analysis of the scattering spectrum<sup>13–16</sup> then permits scattering intensities to be related in a quantitative fashion to unitless normal coordinate displacements ( $\Delta$ ).

In preliminary reports,<sup>17,18</sup> an approximate form of the scattering theory was used to estimate coordinate displacements and mode-specific contributions to reorganization energies for reactions (I) and (II). Here we employ a more



sophisticated and complete form of the theory<sup>16</sup> to obtain much more accurate estimates of displacement and reorganizational or barrier effects for each of the 13 vibrational modes involved in the charge-transfer process. For this uniquely well described system we then employ a complete multi-mode quantum rate theory<sup>20–22</sup> to understand in a quantitative sense the role of every Franck–Condon-active vibration in defining the electrochemical-exchange kinetics. Particular attention is paid here to so-called nuclear tunnelling effects that can arise when thermal activation of specific vibrations is encumbered. Finally, we employ the rate theory to understand how specific vibrational reorganizational effects, together with solvent effects, can influence the temperature dependence and the potential dependence of the electrochemical reaction rate.

## Results and Discussion

### Vibrational displacements and mode-specific reorganizational contributions

Electronic transitions, such as reaction (II), are necessarily accompanied by a redistribution of charge which: (a) induces normal coordinate displacements, and (b) causes local changes in polarizability. From the time-dependent theory of Raman scattering, the relationship between the polarizability tensor for resonant or near-resonant scattering,  $\alpha_{fi}$ , and the coordinate displacement,  $\Delta_k$ , for mode  $k$  is given by the half-Fourier transform of the overlap of a wave packet,  $\phi(t)$ , moving on the upper potential energy surface (Fig. 1) and a vibrational wave function,  $\phi_f$ , on the lower surface:<sup>15,16</sup>

$$\alpha_{fi} = \frac{2\pi i}{h} \int_0^\infty \langle \phi | \phi(t) \rangle \exp(i\omega t - \Gamma t - i\chi_s t - \chi_s k T t^2) dt \quad (2)$$

where

$$\begin{aligned} \langle \phi | \phi(t) \rangle = & \prod_k \left\{ \exp \left\{ -\frac{\Delta_k^2}{2} [1 - \exp(-i\omega_k t)] - \frac{i\omega_k t}{2} \right\} \right. \\ & \times [1 - \exp(-i\omega_k t)]^{n_k} \\ & \times \frac{(-1)^{n_k} \Delta_k^{n_k}}{(2^{n_k} n_k!)^{1/2}} \exp(-iE_{00} t) \end{aligned} \quad (3)$$

In the equations,  $h$  is Planck's constant,  $t$  is time,  $\omega$  is  $2\pi$  times the incident frequency,  $\omega_k$  is the  $2\pi$  times the mode frequency,  $E_{00}$  is the electronic gap,  $n(k)$  is the vibrational quantum number of the  $k$ th mode on the ground electronic surface, and

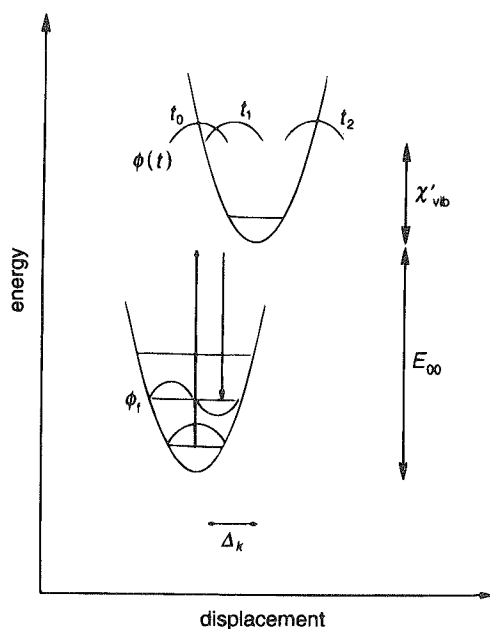


Fig. 1 Time-dependent representation of near-resonant Raman scattering

$\Gamma$  is a homogeneous damping term (dephasing term), which acts to kill the wavepacket on the excited-state surface. Following Myers,<sup>16</sup> two terms involving  $\chi_s(\text{optical})$  [the solvent reorganization energy for reaction (II)] and the temperature have been added to eqn. (2). The first term (real term) acts as an inhomogeneous broadening or damping term (similar to  $\Gamma$ ), and the second term (imaginary term) acts as an energy shift (since the solvent modes have Franck–Condon activity).

For eqn. (2) and (3), the connection to experimental observables comes from the square root relationship between scattering intensities and tensor elements. In addition, as noted by Heller,<sup>13</sup> the full Fourier transform of the vibrational overlap yields the absorption spectrum, which, of course, is also experimentally accessible. To determine displacements for reactions (I) and (II), we made use of the previously reported relative scattering intensities,  $I_k$ , and the charge-transfer absorption spectrum shown in Fig. 2 (solid and dashed lines). Simultaneous fitting yielded the displacement parameters listed in Table 1, the relative scattering intensities shown in Fig. 3 and the absorption spectrum (dashed line) shown in Fig. 2. [In generating the fits, we treated  $E_{00}$  and  $\chi_s(\text{optical})$  as adjustable parameters and assumed that the electronic dephasing effects, described by  $\Gamma$ , were small. While very good fits to the experimental scattering spectrum could be obtained for a range of energy gaps and solvent reorganization energies, we found that the quality of the fit to the experimental adsorption

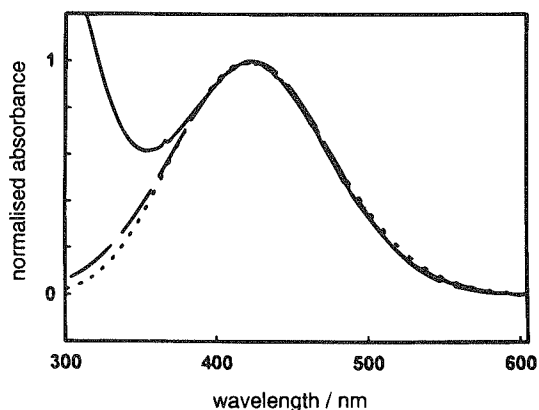


Fig. 2 Normalized absorption spectrum for 4-cyano-*N*-methylpyridinium iodide. Solid line experimental spectrum. Dotted line: gaussian fit to the lowest energy charge-transfer component of the spectrum [reaction (II)]. Dashed line: spectrum obtained from time-dependent theory with  $E_{00} = 15800 \text{ cm}^{-1}$ ,  $\chi_s(\text{optical}) = 1500 \text{ cm}^{-1}$  ( $18 \text{ kJ mol}^{-1}$ ),  $\Gamma = 10 \text{ cm}^{-1}$  and  $\Delta$  values from Table 1.

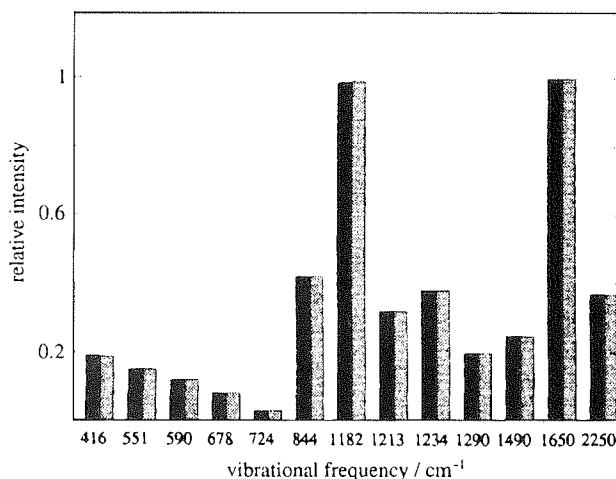


Fig. 3 Normalized experimental Raman scattering intensities (dark columns) and calculated scattering intensities (light columns) for 4-cyano-*N*-methylpyridinium iodide based on 514.5 nm excitation

**Table 1** Vibrational and reorganizational parameters for 4-cyano-*N*-methylpyridinium reduction

mode frequency/cm <sup>-1</sup>	relative scattering intensity	Δ	χ' vib/kJ mol <sup>-1</sup>	assignment
1650	1.00	1.19	14.1	ν(C≡C)
1490	0.25	0.64	3.6	δ <sub>as</sub> (CH <sub>3</sub> )
1290	0.20	0.64	3.1	ν(N-CH <sub>3</sub> )
1234	0.38	0.91	6.2	ν(C=NCH <sub>3</sub> )
1213	0.32	0.85	5.2	δ(C-H) (ring)
1182	0.99	1.53	16.5	(ring breathing)
844	0.42	1.32	8.9	δ(C-H) (ring)
724	0.03	0.10	0.7	γ(C-H) (ring)
678	0.08	0.69	1.9	γ(C-H) (ring)
590	0.12	0.97	3.4	γ(C=NCH <sub>3</sub> )
551	0.15	1.16	4.4	δ(C=N=C)
416	0.19	1.69	7.1	γ(CH <sub>3</sub> )
		total	79.9	

spectrum was much more sensitive to these parameters. [The reported displacement data reflect the Raman fitting obtained by using the 'best' set of  $E_{00}$  and  $\chi_s$ (optical) values.] Mode-specific contributions to the vibrational reorganizational energy (Table 1) were obtained from unitless normal coordinate displacements by using eqn. (4). The total

$$\chi'_{\text{vib}} = 0.5\Delta^2\nu \quad (4)$$

vibrational reorganization energy for reaction (II), or equivalently reaction (I), is 6700 cm<sup>-1</sup> (80 kJ mol<sup>-1</sup>) and is given by the sum of  $\chi'_{\text{vib}}$  values.

A comparison of the data in Table 1 to previously reported results<sup>17</sup> reveals both similarities and differences. The most important differences are a greater role, in Table 1, for high frequency modes and a greater total vibrational reorganization energy (*ca.* 20% greater than previously estimated). The differences primarily reflect limitations in the approximate 'Savin's rule' analysis used earlier. This analysis emphasizes the  $\Delta^2$  scaling of intensities suggested by eqn. (3), but neglects the rather complex interplay between overlap terms implied by the product function in eqn. (3). Also contributing to parameter differences is the specific treatment of solvent reorganizational and broadening effects (dephasing effects) in eqn. (2),<sup>16</sup> but not in the earlier analysis. In any case, the current results should be regarded as more accurate.

Finally, we note that the connection between normal coordinate displacements [unitless and bond-length changes (local coordinate displacements having units of distance) can be complex. For example, the normal mode at  $\nu = 1182$  cm<sup>-1</sup> in Table 1 involves simultaneous changes in two C-N and four C-C bonds.)] Occasionally, however, symmetry or other factors can render local and normal modes physically equivalent. Under these conditions, the two types of displacement parameters can be interconverted *via* eqn. (5):

$$|\Delta a| = (\Delta^2 h / \mu \nu b)^{1/2} \quad (5)$$

where  $\mu$  is a reduced mass.

**Classical rate calculations.** To place subsequent multimode quantum rate simulations in context, we start with a classical Marcus-type interfacial rate calculation with acetonitrile as solvent. To motivate the calculation we assume that the reaction site is the outer Helmholtz plane, the reaction kinetics are marginally non-adiabatic at 298 K and that the inverse of the longitudinal relaxation time of the solvent (acetonitrile<sup>23</sup>) is an acceptable dynamical benchmark. We recognize that each of these assumptions is open to criticism. However, since our real interest here is mode-specific vibrational rate effects, we require only that the assumptions be reasonable enough to provide a basis for relative comparisons of various representations of vibrational barrier and kinetic effects.

According to classical ET theory, the rate constant ( $k_{\text{ET}}$ ) for non-adiabatic, outer-sphere electron transfer at an electro-

chemical interface can be expressed as:<sup>8</sup>

$$k_{\text{ET}} = \delta d (4\pi^2 H_{12}^2 / h) (4\pi\chi RT)^{-1/2} \exp[-\Delta G^*(\text{class})/RT] \quad (6)$$

where

$$\Delta G^*(\text{class}) = [(F/RT)(E_f - E) + \chi]^2 / 4\chi \quad (7)$$

In the equations,  $\delta d$  is an effective reaction zone thickness (taken as 0.6 Å),<sup>24</sup>  $H_{12}$  is an electronic coupling matrix element,  $F$  is the Faraday constant,  $E$  is the electrochemical potential,  $E_f$  is the formal potential and  $\chi$  is the total reorganization energy. The non-adiabaticity assumption (above) yields  $4 \times 10^{12}$  s<sup>-1</sup> for the product of the two quantities in parentheses in the pre-exponential portion of eqn. (6). [The parameters needed to generate this (arbitrary) value are  $H_{12} = 130$  cm<sup>-1</sup> and  $\chi = 9700$  cm<sup>-1</sup> (116 kJ mol<sup>-1</sup>).] Fig. 4 illustrates the relationships among the classical parameters.

To estimate the solvational component of  $\chi$  we again assume that Marcus theory is applicable.<sup>6</sup>

$$\chi_s = \left(\frac{e^2}{2}\right) \left(\frac{1}{r} - \frac{1}{R_i}\right) \left(\frac{1}{D_{\text{op}}} - \frac{1}{D_s}\right) \quad (8)$$

In eqn. (8),  $e$  is the unit electronic charge,  $r$  is the reactant radius,  $R_i$  is the distance from the charged reactant to a corresponding image charge in the electrode,  $D_s$  is the static relative permittivity of the solvent and  $n$  is its refractive index. The reactant in reaction (I) is poorly represented as a sphere. Nevertheless, in order to utilize eqn. (8) we estimated the effective radius as the cube root of the product of the radii in the

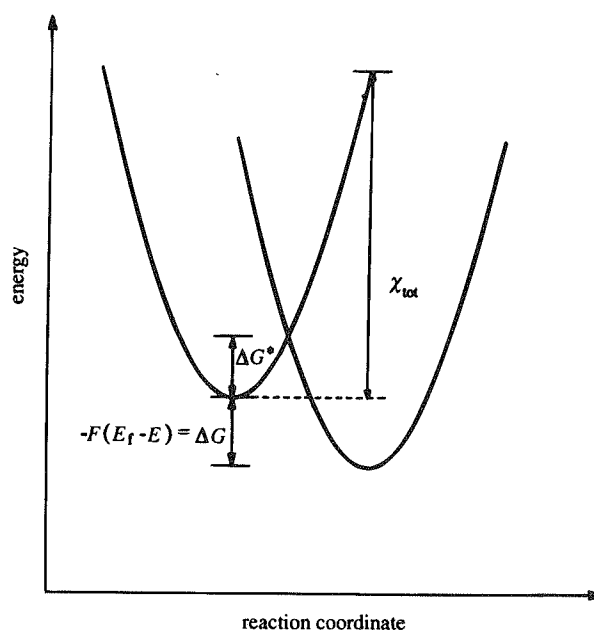


**Fig. 4** Schematic representation of relationships between classical energy and displacement parameters

x-, y- and z-directions.<sup>25,26</sup> The value obtained was 2.2 Å. To estimate  $R_1$  we assumed a closest approach distance with the 4-cyano-*N*-methylpyridinium ion coplanar to the electrode surface, but separated from the surface by a chemisorbed layer of acetonitrile. These assumptions yielded  $R_1 = 11$  Å and  $\chi_s = 3000$  cm<sup>-1</sup> (36 kJ mol<sup>-1</sup>). [Note that the solvent reorganization energy estimated here for the electrochemical reaction differs (as expected) from the  $\chi_s$  value obtained above for the optical reaction. Note also that the applicability of the imaging correction is open to question. If it is omitted,  $\chi_s$  increases slightly (*ca.* 17%). In the present context, since we are less interested in obtaining an exact value for  $\chi_s$  than in obtaining a reasonable value that will subsequently permit us to examine vibrational effects, we will forego any further consideration of the relative merits of alternative solvation models.]

If only solvent reorganization is considered, eqn. (6) yields a standard rate constant of 1150 cm s<sup>-1</sup> and the rate *vs.* driving force behaviour shown in Fig. 5 (solid curve). Addition of the Raman-derived vibrational reorganization energy, however, has an enormous effect: the standard rate constant decreases to 0.20 cm s<sup>-1</sup> and the rate *vs.* driving force behaviour now is described by the dashed curve in Fig. 5. Note that at high driving forces, both calculations predict an eventual decrease of rate with increasing driving force. As pointed out some time ago by Marcus,<sup>6,27</sup> the availability of a continuum of filled states below the Fermi level (*i.e.*, more positive than the applied potential) will prevent the observation of inverted behaviour at a metal electrode/solution interface. Instead, the  $k_{ET}$  *vs.* overpotential response will be given by an integration of rates over the available donor levels.<sup>4,28</sup>

$$k_{ET} = \text{constant} \times \rho_{elec} \int_{-\infty}^{\infty} \exp[-\Delta G^*(E)/RT] \times \{1 + \exp[(E_{fermi} - E)/RT]\}^{-1} dE \quad (9)$$

where  $\rho_{elec}$  is the density of electronic states in the electrode. Eqn. (9) differs slightly from the equation presented by Chidsey<sup>4</sup> and by Weber and Creager<sup>28</sup> in that it makes no specific assumptions about the form of the rate constant *vs.* overpotential (or driving force) relationship. Also, it employs an electrochemical sign convention, rather than the usual vacuum sign convention, for the energy terms.

Eqn. (9) was implemented by using a standard 'trapezoid rule' approach. Note that the absolute numerical value of the integrated rate response depends on the value chosen for  $\rho_{elec}$ . Since we have no particular knowledge of  $\rho_{elec}$  and since our focus, in any case, is on Franck-Condon rather than electronic phenomena, we simply normalized rate constants from eqn. (9) to the  $k_{ET}$  value given by eqn. (6) at  $E = E_f$ . Fig. 6 shows that the effect of the integration is to enhance reactivity

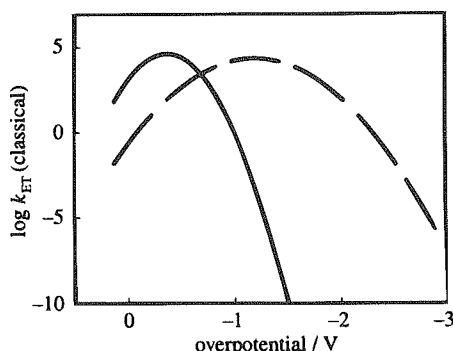


Fig. 5 Calculated classical rate constant *vs.* driving force curves [eqn. (6)] for reaction (I). Solid line: behaviour with solvent reorganization only. Dashed line: behaviour with both solvent and internal vibrational reorganization. Reorganizational parameters:  $\chi_s = 3000$  cm<sup>-1</sup> (36 kJ mol<sup>-1</sup>),  $\chi_{vib} = 6700$  cm<sup>-1</sup> (79.9 kJ mol<sup>-1</sup>).

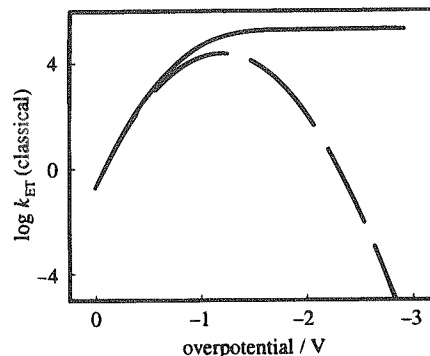


Fig. 6 Calculated classical rate constant *vs.* driving force curves for reaction (I), assuming reorganization of both solvent and interval vibrational modes. Dashed line: electron transfer exclusively from states at the Fermi level [eqn. (6)]. Solid line: electron transfer from all available states [eqn. (9)]. (Curves are arbitrarily normalized at  $E = E_f$ .) Reorganizational parameters:  $\chi_s = 3000$  cm<sup>-1</sup> (36 kJ mol<sup>-1</sup>),  $\chi_{vib} = 6700$  cm<sup>-1</sup> (79.9 kJ mol<sup>-1</sup>).

preferentially at high driving forces and to eliminate the rate inversion effect.

**Multi-mode quantum rate calculations. 1 Golden rule formulation.** A mode-specific evaluation of interfacial ET reactivity requires a quantum mechanical or 'spectroscopic' formulation of the rate equation. For non-adiabatic reactions, the essence of this approach is Fermi's golden rule, which states that the first-order rate constant (in this case, the rate constant for the reaction after the reactant has been positioned at the outer Helmholtz plane) will vary as the square of the initial-state [left hand side of reaction (I)]/final-state [right hand side of reaction (I)] electronic overlap,  $H_{12}$ , and a weighted density of final vibronic states (*i.e.*, number of final states per unit of energy),  $\rho_{vib}$ :<sup>29</sup>

$$ET \text{ rate constant} = (4\pi^2 H_{12}^2 / h) \rho_{vib} \quad (10)$$

In eqn. (10), the weighting factor is the square of the overlap of the wavefunctions,  $X$ , for the initial vibrational state,  $1v$ , and a manifold of final vibrational states,  $2w$ :

$$\rho_{vib} = \sum_w |\langle X_{1v} | X_{2w} \rangle|^2 \delta(\epsilon_{1v} - \epsilon_{2w}) \quad (11)$$

where  $\epsilon_{1v}$  and  $\epsilon_{2w}$  are energies of specific vibrational levels and  $\delta$  now is the Dirac delta function. If the initial state is thermally equilibrated then a range of vibrational levels will be populated and the golden rule can be rewritten in more explicit form as:<sup>22,29,30</sup>

$$ET \text{ rate constant} = \left( \frac{4\pi^2 H_{12}^2}{h} \right) Q_1^{-1} \sum_v \sum_w \times \exp\left(-\frac{\epsilon_{1v}}{RT}\right) |\langle X_{1v} | X_{2w} \rangle|^2 \delta(\epsilon_{1v} - \epsilon_{2w}) \quad (12)$$

where  $Q_1$  is defined as:

$$Q_1 = \sum_v \exp\left(-\frac{\epsilon_{1v}}{RT}\right) \quad (13)$$

Fig. 7 provides a schematic representation of the vibrational overlap component of eqn. (11) for the simple case where only one mode is displaced. [For a multi-mode representation of squared overlaps (unitless Franck-Condon factors) see eqn. (14), below.] From the figure, the best vibrational overlap (or largest Franck-Condon factor) is obtained at the intersection point of the classical potential energy surfaces. Note, however, that finite overlaps also occur at energies below the intersection region. From eqn. (10), therefore, ET will occur both at the classical crossing point [ $\Delta G^*(\text{class})$ ] and at lower (and higher) energies. Note further that while the overlap criterion

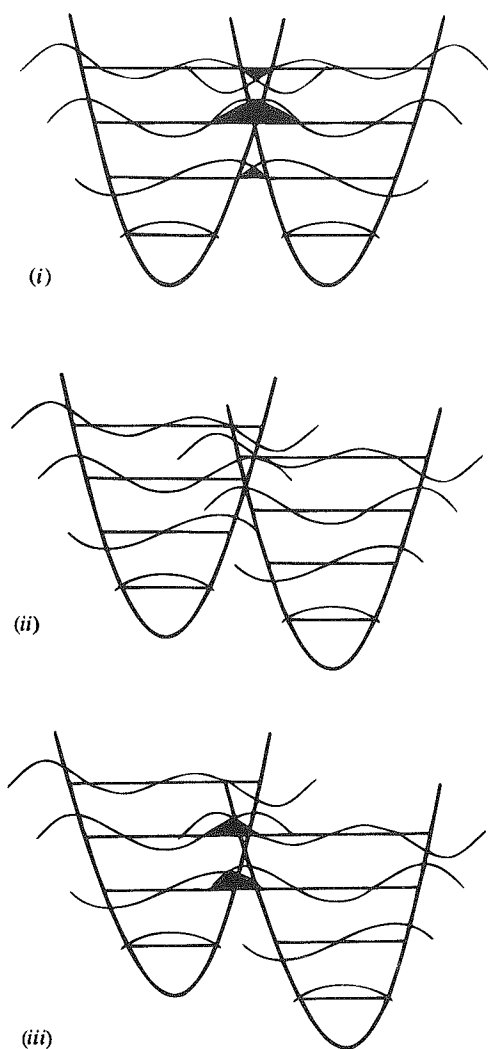


Fig. 7 Schematic representation of initial state/final state vibrational overlaps at: (i)  $E = E_r$ , (ii)  $E = E_r - 0.5(F/RT)v$  and (iii)  $E = E_r - (F/RT)v$ .

will favour ET at the classical intersection point, the crossing probability is also necessarily weighted by the Boltzmann population of the vibrational state. Boltzmann or thermal effects, therefore, will usually favour crossing at energies below the intersection point. From this perspective, the essence of the classical theory is the approximation that Franck-Condon factors are unity at the classical intersection point and zero at all other energies. If the approximation is completely satisfied then the thermally averaged Franck-Condon factor,  $FC$ , can be equated with  $\exp[-\Delta G^*(\text{class})/RT]$ . To the extent that the approximation is not satisfied: (a)  $FC$ , under exchange conditions, will exceed  $\exp[-\Delta G^*(\text{class})/RT]$  and (b) the quantum ET rate constant, under exchange conditions, will exceed the classical rate constant.

An additional element of eqn. (10) and (11) is the requirement that energy be conserved (note the delta function . . .) during the crossing process. This, in turn, implies that energy matching for initial and final vibrational states must be accomplished. In Fig. 7, energy matching is achieved in cases (i) and (iii), but not (ii). In case (ii), therefore, ET should shut off and remain off until the driving force is sufficient [cf. case (iii)] to bring the vibrational levels back into resonance. Fig. 8 shows the hypothetical behaviour [after application of eqn. (8)] of a single-mode system involving essentially no solvent reorganization. {Eqn. (9) was employed with  $FC(E)$  in place of  $\exp[-\Delta G^*(E)/RT]$ .} Note that well-defined steps occur in the rate constant *vs.* driving force plot in energy increments corresponding to the vibrational spacing in Fig. 7.

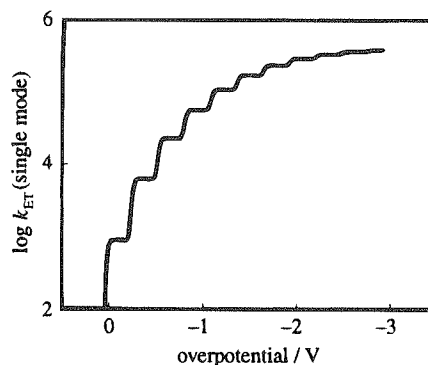


Fig. 8 Calculated sum-over-states rate constant *vs.* driving force behaviour [eqn. (9), (10) and (14)] for a hypothetical single-mode system featuring  $\nu = 2250 \text{ cm}^{-1}$ ,  $\Delta = 3.5$ ,  $\chi_s = 0.5 \text{ kJ mol}^{-1}$  ( $\approx 0 \text{ kJ mol}^{-1}$ ) and reaction zone and pre-exponential factors of  $6 \times 10^{-9} \text{ cm}$  and  $4 \times 10^{12} \text{ s}^{-1}$ , respectively.

In real systems, energy mismatches (and structure in the log  $k_{ET}$  *vs.*  $E$  plot) can be overcome *via* involvement of a thermally equilibrated solvent having a quasi-continuum of energy levels. Extension of the reaction of cases where two, three or  $n$  vibrational modes participate implies the extension of Fig. 7 to three, four or  $n + 1$  dimensions. Energy sharing among the many modes to be activated then provides an additional mechanism for achieving energy matching.

**2 Implementation.** To implement the golden rule approach for the reduction of 4-cyano-*N*-methylpyridinium, we make use of the formulation of Jortner and Bixon<sup>20</sup> for  $\rho_{vib}$  as described further by Brunschwig and Sutin<sup>22</sup> and by Spears *et al.*<sup>31</sup>

$$\rho_{vib} = \underbrace{(4\pi\chi_s kT)^{-1/2}}_{(a)} \underbrace{\exp\left\{-\left[\sum_j S_j \coth(h\nu_j/2kT)\right]\right\}}_{(b)} \underbrace{\times \prod_j \sum_{m_j=-\infty}^{+\infty} \exp(m_j h\nu_j/kT) I_{|m_j|}[S_j \text{csch}(h\nu_j/2kT)]}_{(c)} \underbrace{\times \exp\left[-\frac{(\Delta E + \chi_s + \sum_i m_i h\nu_i)^2}{4\chi_s RT}\right]}_{(d)} \quad (14)$$

In eqn. (14),  $S$  equals  $\Delta^2/2$ ,  $m$  is the change in vibrational quantum number and  $I_m$  is a modified Bessel function of order  $m$  (where the Bessel function serves as an approximation to some rather intricate ladder operators<sup>32</sup> required to obtain correct Franck-Condon sums).  $\Delta E$  is the energy of the final state minus the energy of the initial state and can be equated, after units conversion, with the overpotential for an electrochemical reduction reaction. The first and third summations and the product term encompass all modes (other than classical solvent modes) that are Franck-Condon active. The quantum number summation (second summation) technically is infinite, but generally converges if levels from  $-10$  to  $+10$  are considered. (Computational cut-off criteria permitted us to evaluate an even smaller range of  $m$  values in several cases.) The overall form of eqn. (14) obviously is fairly complicated. Briefly, however, terms (b) and (c) collectively describe how vibrational overlaps in a fully thermally equilibrated, multi-mode system depend on vibrational displacement, frequency, quantum number and temperature; term (d) describes energy matching (energy conservation) effects, including solvent broadening effects. In the classical theory [eqn. (6)] term (a) is a component of the electronic prefactor and arises in a straightforward way from Landau-Zener theory.<sup>30,33,34</sup> Curiously, however, the same term in the quantum treatment is

better viewed as a component of the vibrational density of states parameter [eqn. (11)].<sup>22</sup>

To obtain interfacial ET rate constants we have assumed that eqn. (6) can be adopted, but with quantum parameters [eqn. (14)] replacing the classical parameters:

$$k_{\text{ET}} = \delta r (4\pi^2 H_{12}^2 / \hbar) \rho_{\text{vib}} \quad (15)$$

While programs based on eqn. (14) and (15) can be extended to include an arbitrarily large number of modes,  $j$ , we encountered unacceptably long computational times when  $j$  exceeded five or six. To reduce the computational time, modes of similar frequency were grouped and averaged. Displacements for each of the resulting composite modes were then adjusted such that their contributions to the reorganization energy each equalled the sum of the contributions of the pertinent individual modes to the reorganization energy. For each group of modes, rate calculations were then run with and without averaging in order to verify that averaging did not affect computational outcomes. [Obviously, continuing improvements in computer performance can be expected to decrease the need for mode averaging in future studies, however, because the computational time scales roughly as the factorial of the product of the number of modes evaluated and the number of quantum number changes considered per mode, it is unlikely that mode averaging for large systems (greater than a dozen modes) can be altogether eliminated in the near future.]

**3 Results.** Fig. 9 (dashed line) shows the dependence of the fully quantum mechanical rate constant [ $k_{\text{ET}}$ , eqn. (15)] on driving force, where the plot was constructed by using five blended vibrational modes and one fully classical mode (solvent mode). In contrast to the corresponding classical rate plots in Fig. 5, this plot displays a marked driving-force asymmetry, *i.e.*, a much weaker dependence of  $k_{\text{ET}}$  on  $\Delta E$  in the inverted region than in the normal region. The solid line in Fig. 9 shows the dependence of the quantum mechanical rate constant on driving force after accounting for so-called 'sum-over-states' effects [eqn. (9)]. To understand how specific modes affect reactivity, several additional calculations were performed under exchange conditions (zero overpotential). In the calculations, modes were progressively eliminated and the rate was re-evaluated. The ratio of rates without and with the desired mode then yielded a rate attenuation factor for that mode. Table 2 shows that: (i) all Raman active modes exert a rate attenuation effect, (ii) the attenuation effects scale roughly with the mode specific reorganization energy and (iii) the largest single attenuation effect (*ca.* factor of 3) comes from a ring-based C=C stretching mode at 1650  $\text{cm}^{-1}$ . Thus, no single vibration exerts a dominant rate attenuation effect,

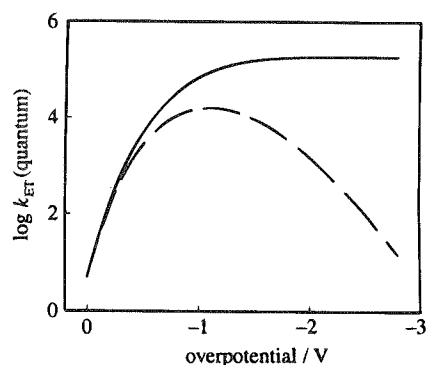


**Fig. 9** Calculated multi-mode quantum mechanical rate constant *vs.* driving force curves for reaction (I). Dashed line: electron transfer exclusively from states at the Fermi level. Solid line: electron transfer from all available states. Reorganizational parameters:  $\chi_s = 3000 \text{ cm}^{-1}$  (36  $\text{kJ mol}^{-1}$ ); normal coordinate displacements and  $\chi_{\text{vib}}$  values taken from Table 1.

although collectively the 13 vibrations exert a very substantial effect. Finally, an additional comparison shows (reassuringly) that when all vibrational reorganizational contributions are eliminated, the calculated quantum rate constant fully converges to the 'solvent only' classical rate constant of 1150  $\text{cm s}^{-1}$ , described above. (The 'solvent only' quantum calculation was carried out by using dummy modes having infinitesimal displacements and, therefore, infinitesimal  $\chi_{\text{vib}}$  values.)

Returning to the rate *vs.* driving force curves in Fig. 9, the asymmetry in the dashed curve is a clear computational manifestation of enhanced nuclear tunnelling effects in the inverted region. While the sum-over-states integration largely masks these effects, other manifestations of non-classical behaviour exist. Most notably, the quantum mechanical exchange rate constant (5.0  $\text{cm s}^{-1}$ ) exceeds the classical exchange rate constant by a factor of 25. Again, the rate enhancement effect can be interpreted as a nuclear tunnelling phenomenon. This effect was further explored by performing calculations as a function of temperature. The calculations are summarized in Fig. 10 in the form of modified Eyring plots ( $T^{1/2}$  pre-factor variation). The slopes of the plots, when multiplied by  $-1/R$ , yield effective activation enthalpies. Particularly noteworthy are: (i) the strong temperature dependence of the quantum mechanical activation enthalpy (albeit, largely at experimentally inaccessible temperatures), and (ii) the much smaller value, even at room temperature, for  $\Delta H^*$  (quantum) in comparison with  $\Delta H^*$  (classical). The enthalpy parameter when combined with the exchange rate constant also yields, in the quantum mechanical case, an apparent activation entropy equalling  $-24 \text{ J}$

**Table 2** Mode-specific kinetic parameters for 4-cyano-*N*-methylpyridinium reduction

mode frequency/ $\text{cm}^{-1}$	rate-attenuation factor	isolated nuclear tunnelling factor <sup>a</sup>	sequential nuclear tunnelling factor <sup>b</sup>
416	2.04	1.07	1.07
551	1.51	1.07	1.07
590	1.38	1.06	1.05
678	1.19	1.04	1.03
724	1.09	1.02	1.00
844	2.06	1.29	1.29
1182	2.88	2.02	2.35
1213	1.42	1.26	1.10
1234	1.48	1.33	1.32
1290	1.22	1.16	1.15
1490	1.30	1.22	1.31
1650	2.01	1.36	2.21
2250	1.20	1.41	1.40
total product:	230	15	25

<sup>a</sup> Calculated by making only a single mode behave classically (see text). <sup>b</sup> Calculated by progressively converting quantum mechanical modes to classical modes and determining incremental tunnelling effects.

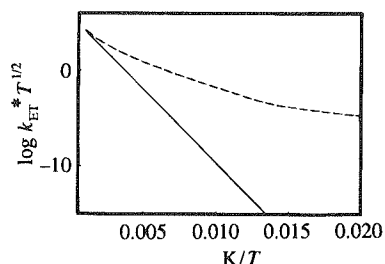


**Fig. 10** Modified Eyring plots for reaction (I) based on sum-over-states classical (solid line) and multi-mode quantum mechanical (dashed line) rate constant calculations. At 298 K the slopes of the plots yield effective classical and quantum mechanical activation enthalpies of 29 and 14 kJ mol<sup>-1</sup>, respectively. Reorganizational parameters identical to those in Fig. 9.

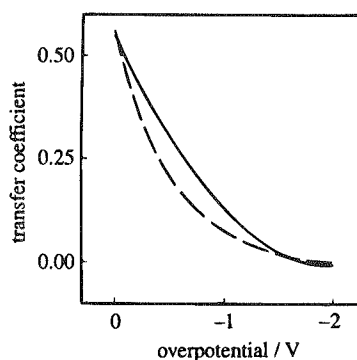


**Fig. 11** Dependence of calculated classical (solid line) and quantum mechanical (dashed line) transfer coefficients on overpotential at 298 K. Reorganizational parameters identical to those in Fig. 9.

K<sup>-1</sup> mol<sup>-1</sup> at 298 K. (The apparent activation entropy is zero in the classical case.) Negative apparent activation entropies, when obtained at  $E = E_f$ , typically are interpreted as non-adiabaticity factors (*i.e.*, factors reflecting inefficient electron tunnelling). Here, however, the apparent activation entropy is associated strictly with the Franck–Condon sums and must be regarded, therefore, as a nuclear tunnelling effect.

One further manifestation of the tunnelling effect is a slight perturbation of the calculated transfer coefficient,  $\alpha$  [defined as  $(-RT/F)d \log(k_{ET})/dE$ ]. At 298 K, under exchange conditions and without rate integration, both  $\alpha$ (classical) and  $\alpha$ (quantum mechanical) are necessarily 0.5 (since we have neglected any oxidation-state-dependent changes in vibrational frequencies). After sum-over-states integration [eqn. (9)] both calculations yield transfer coefficients of slightly greater than 0.5 at  $E = E_f$ . Again since oxidation-state-dependent changes in vibrational frequencies have been neglected,  $\log k_{ET}$  *vs.*  $E$  plots for the reverse reaction (*i.e.*, oxidation) are mirror images of those for the reduction reaction and calculated transfer coefficients for the oxidation reaction are also greater than 0.5. This leads to the somewhat worrisome result that the sum of oxidative and reductive transfer coefficients, calculated at the same potential, exceeds the number of electrons transferred—a finding that is generally regarded as impossible because it ultimately implies violation of microscopic reversibility at potentials other than the formal potential. Further consideration of Fig. 8 and 9 and eqn. (9) provides some insight: the axes labelled as overpotential or driving force actually describe the energy difference between the Fermi level (applied potential) and the formal potential. Because rate contributions are summed over all electronic states, however, the average driving force is always somewhat less than the driving force implied by the figures. Thus at an applied potential equalling  $E_f$ , the reduction reaction, on average, occurs at a potential slightly positive of  $E_f$ ; the oxidation reaction occurs, on average, at a different potential that is slightly negative of  $E_f$ .

Returning to tunnelling effects, Fig. 11 shows that at high driving forces  $\alpha$  (quantum mechanical) and  $\alpha$ (classical) both approach zero. In the intermediate region, however, the two transfer coefficients differ. The differences suggest a caveat for related experimental studies where the reorganization energies are derived from fits of the shapes of the  $\log k_{ET}$  *vs.* overpotential curves.<sup>4,28,35–38</sup> The assumed fitting function is generally the classical Marcus response [eqn. (7) and (9)]. The range of the fit is typically limited (by experiment) to the lower half or two thirds of the rate-constant plot. While most of the systems examined in this way have indeed been largely classical (*i.e.*, dominated by solvent reorganization and, therefore, adequately characterized by this approach),<sup>4,28,35–38</sup> we suggest more generally that the fitting strategy may lead to errors when significant nuclear tunnelling effects and high-frequency Franck–Condon activity exist.

To pinpoint the origins of the non-classical rate effects we carried out several additional ambient temperature calculations. In each of these calculations, a specific (non-blended) mode from Table 1 was included as a sixth vibrational mode in the quantum mechanical rate calculation, while conserving the total reorganization energy. The isolated mode was then made fully classical (*i.e.*, combined with  $\chi_s$ ) and the rate constant was recalculated. The ratio of the fully quantum mechanical rate constant to the partially quantum mechanical rate constant (Table 2) was then taken as a measure of the mode-specific contribution to the non-classical rate effect (nuclear tunnelling effect). (Hence each calculation involved effectively 12 quantum modes and one classical mode.) Inspection of the table shows: (i) that significant non-classical effects are observed only for medium to high frequency vibrational modes, but (ii) not all such modes contribute significantly. Indeed, further comparison shows that in addition to high frequencies, large reorganizational effects (Table 1) are required in order for modes to provide significant nuclear tunnelling contributions.

Additional analysis shows that the product of mode-specific tunnelling factors in Table 2 yields a total tunnelling factor of 15, *i.e.*, somewhat less than the factor of 25 expected from the ratio of  $k_{ET}$ (quantum mechanical) to  $k_{ET}$ (classical). The origin of the discrepancy lies in the way prefactors [ $\chi_s^{-1/2}$  terms in eqn. (6) and (14)] change when isolated quantum modes are made classical *vs.* the behaviour obtained when all quantum modes are made classical. In light of the discrepancy, mode-specific tunnelling effects were also evaluated by progressively converting quantum modes to classical modes, beginning with the lowest frequency mode. The results are listed in Table 2. When calculated in this way, the product of the mode-specific tunnelling factors does yield 25 for the total tunnelling factor. The tunnelling contribution ascribed to a particular mode, however, is now slightly dependent upon the order in which the modes are considered.

Finally, we note that the tunnelling terminology implies a finite activation barrier penetration probability. Barrier penetration is most probable when the reduced mass of the tunnelling entity (*e.g.*, a particular atom or group of atoms within the molecule) is small and the corresponding vibrational frequency is large. An alternative but equivalent view emphasizes the dependence of the vibrational wavefunction shapes and, therefore, overlaps, on vibrational frequency. Fig. 12 illustrates the idea for a pair of hypothetical single-mode reactions having identical classical activation barrier heights and reorganization energies, but very different mode frequencies. In both cases the lowest vibrational wavefunctions are centred on the minimum on the classical reactant or product potential-energy surface. The wavefunctions for the low-frequency vibration, however, are much more strongly localized than those for the high-frequency vibration. Consequently, very little initial-state/final-state vibrational

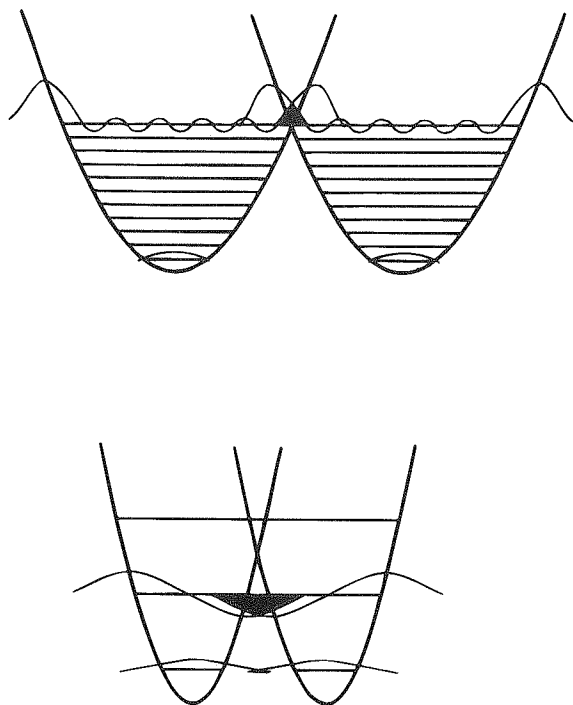


Fig. 12 Schematic representation of vibrational overlaps for high frequency (top diagram) and low frequency (bottom diagram) systems

overlap is obtained at this level and reactivity is achieved only after classical activation. For the high-frequency system, on the other hand, the wavefunctions are much more diffuse. It follows that significant overlap and, therefore, significant reactivity, can be obtained even in the absence of activation. From a spectroscopic perspective, therefore, net reactivity (finite overlap) without full thermal activation is the basis for the non-classical ET rate effect.

## Conclusions

The multi-mode quantum rate analysis clearly illustrates the importance of vibrational reorganizational effects in defining the interfacial reactivity of a representative organic cation-neutral-radical system, 4-cyano-*N*-methylpyridinium<sup>+/0</sup>. For this system, a time-dependent analysis of Raman scattering effects shows that the total vibrational reorganization energy is 6700 cm<sup>-1</sup> (80 kJ mol<sup>-1</sup>) and that the reorganizational effects are distributed over more than 12 distinct modes. Insertion of the reorganizational information into the rate theory leads to an extremely detailed—perhaps unprecedented—description of the kinetic effects induced by internal reorganization. Individual vibrational modes exert anywhere from factor of 1 to 3 attenuation effects upon the calculated exchange rate constant.

Further analysis *via* the quantum rate theory also provides insight into non-classical kinetic effects. The calculated effects include substantial rate accelerations, substantial effective barrier lowering (decreased Eyring slope) and significantly diminished transfer coefficients. A mode specific analysis shows that the largest single calculated contribution to the non-classical rate behaviour comes from a C≡C stretching mode, which is characterized by both a large displacement and a high vibrational frequency. Finally, while the time-dependent analysis is by no means general, we believe that it can be profitably applied to a substantial number of interfacial electron transfer reactions. Indeed, we intend to report

shortly on related reactions involving hexacyanoferrate(III) and nitrobenzene reduction at semiconductor/solution interfaces and hexamethylbenzene oxidation at the metal/solution interface.

We thank Professor Ken Spears for several helpful discussions regarding programming and for providing a version of the multi-mode rate code. We also acknowledge helpful discussions with Dr. Bruce Brunschwig, Professor Steve Creager and Professor Chris Chidsey. We thank the Office of Naval Research and the DOD AASERT program for support of our work. J.T.H. also gratefully acknowledges unrestricted support from the Dreyfus Foundation (Teacher-Scholar Award, 1991–96).

## References

- W. R. Fawcett, *Angew. Chem., Int. Ed. Engl.*, 1995, **34**, 194.
- M. J. Weaver, *J. Mol. Liq.*, 1994, **60**, 57.
- M. J. Weaver, *Chem. Rev.*, 1992, **92**, 463.
- C. E. D. Chidsey, *Science*, 1991, **251**, 919.
- M. D. Newton, *Chem. Rev.*, 1991, **91**, 767.
- R. A. Marcus, *J. Chem. Phys.*, 1965, **43**, 679.
- N. Sutin, *Prog. Inorg. Chem.*, 1983, **30**, 441.
- M. J. Weaver, in *Comprehensive Chemical Kinetics*, ed. R. G. Compton, 1988, vol. 27.
- J. F. Smalley, C. E. D. Chidsey, S. W. Feldberg, M. D. Newton and Y. P. Liu, *J. Phys. Chem.*, 1995, **99**, 13141.
- J. T. Hupp and X. L. Zhang, *J. Phys. Chem.*, 1995, **99**, 853.
- B. S. Brunschwig, C. Creutz, D. H. Macartney, T.-K. Sham and N. Sutin, *Faraday Discuss. Chem. Soc.*, 1982, **74**, 113.
- J. T. Hupp and M. J. Weaver, *Inorg. Chem.*, 1983, **22**, 2557.
- E. J. Heller, R. L. Sundberg and D. Tannor, *J. Phys. Chem.*, 1982, **86**, 1822.
- A. B. Myers and R. A. Matthies, in *Biological Applications of Raman Spectroscopy*, ed. T. G. Spiro, 1987, vol. 2.
- J. I. Zink and K. S. K. Shin, *Adv. Photochem.*, 1981, **16**, 119.
- A. B. Myers, *Chem. Phys.*, 1994, **180**, 215.
- R. L. Blackburn, C. S. Johnson, J. T. Hupp, M. A. Bryant, R. L. Sobocinski and J. E. Pemberton, *J. Phys. Chem.*, 1991, **95**, 10535.
- C. S. Johnson, *J. Electrochem. Soc.*, 1992, **139**, 58C.
- E. M. Kosower, *J. Am. Chem. Soc.*, 1958, **100**, 5790.
- J. Jortner and M. J. Bixon, *J. Chem. Phys.*, 1988, **88**, 167.
- A. Sarai and T. Kakitani, *Chem. Phys. Lett.*, 1981, **77**, 427.
- B. S. Brunschwig and N. Sutin, *Commun. Inorg. Chem.*, 1987, **6**, 209.
- G. E. McManis and M. J. Weaver, *Chem. Phys.*, 1989, **48**, 452.
- J. T. Hupp and M. J. Weaver, *J. Electroanal. Chem.*, 1983, **152**, 1.
- G. M. Brown and N. Sutin, *J. Am. Chem. Soc.*, 1979, **101**, 883.
- C. A. Koval, M. E. Ketterer and C. M. Reidsma, *J. Phys. Chem.*, 1986, **90**, 4201.
- R. A. Marcus, *Electrochim. Acta*, 1968, **13**, 995.
- K. Weber and S. E. Creager, *Anal. Chem.*, 1994, **66**, 3164.
- P. W. Atkins, *Molecular Quantum Mechanics*, Oxford University Press, Oxford, 2nd edn., 1983, pp. 197–199.
- B. S. Brunschwig, J. Logan, M. D. Newton and N. Sutin, *J. Am. Chem. Soc.*, 1980, **102**, 5798.
- K. G. Spears, X. Wen and S. M. Arrivo, *J. Phys. Chem.*, 1995, **99**, 9693.
- A. Sarai and T. Kakitani, *Chem. Phys. Lett.*, 1981, **77**, 427.
- L. Landau, *Phys. Z. Sowjetunion*, 1932, **2**, 46.
- C. Zener, *Proc. R. Soc. London, Ser. A*, 1932, **137**, 696; 1933, **140**, 660.
- T. M. Nahir, R. A. Clark and E. F. Bowden, *Anal. Chem.*, 1994, **66**, 2595.
- L. Tender, M. T. Carter and R. W. Murray, *Anal. Chem.*, 1994, **66**, 3173.
- H. O. Finklea and D. D. Hanshew, *J. Am. Chem. Soc.*, 1992, **114**, 3173.
- A. M. Becka and C. J. Miller, *J. Phys. Chem.*, 1992, **96**, 2657.

Paper 6/02670B; Received 17th April, 1996